

Ionic Accumulation as a Diagnostic Tool in Perovskite Solar Cells: Characterizing Band Alignment with Rapid Voltage Pulses

Nathan S. Hill, Matthew V. Cowley, Nadja Gluck, Miriam H. Fsadni, Will Clarke, Yinghong Hu, Matthew J. Wolf,* Noel Healy, Marina Freitag, Thomas J. Penfold, Giles Richardson, Alison B. Walker,* Petra J. Cameron,* and Pablo Docampo*


Despite record-breaking devices, interfaces in perovskite solar cells are still poorly understood, inhibiting further progress. Their mixed ionic-electronic nature results in compositional variations at the interfaces, depending on the history of externally applied biases. This makes it difficult to measure the band energy alignment of charge extraction layers accurately. As a result, the field often resorts to a trial-and-error process to optimize these interfaces. Current approaches are typically carried out in a vacuum and on incomplete cells, hence values may not reflect those found in working devices. To address this, a pulsed measurement technique characterizing the electrostatic potential energy drop across the perovskite layer in a functioning device is developed. This method reconstructs the current-voltage (JV) curve for a range of stabilization biases, holding the ion distribution “static” during subsequent rapid voltage pulses. Two different regimes are observed: at low biases, the reconstructed JV curve is “s-shaped”, whereas, at high biases, typical diode-shaped curves are returned. Using drift-diffusion simulations, it is demonstrated that the intersection of the two regimes reflects the band offsets at the interfaces. This approach effectively allows measurements of interfacial energy level alignment in a complete device under illumination and without the need for expensive vacuum equipment.

1. Introduction

Perovskite solar cells (PSCs) have emerged as a serious contender for large-scale solar energy harvesting with demonstrated power conversion efficiencies of 25.2%, nearly matching the best research silicon cell efficiencies.^[1] Lead-halide perovskites exhibit a winning combination of low-cost and abundant constituent elements, solution-processability and outstanding optoelectronic properties. Interface engineering has been a crucial part of the acceleration of device performance. There is a breadth of work on various approaches to improve charge transport dynamics from the perovskite layer, briefly: passivation layers, self-assembled monolayers, inverted architectures, and novel transport materials.^[2–4] Historically, this work has been conducted by a trial-and-error approach when developing novel materials and surface modifications which is cumbersome, slow,

N. S. Hill, N. Healy
School of Mathematics
Statistics and Physics
Newcastle University
Herschel Building, Newcastle upon Tyne NE1 7RU, UK

M. V. Cowley, P. J. Cameron
Centre for Sustainable and Circular Technologies
Department of Chemistry
University of Bath
Claverton Down, Bath BA2 7AY, UK
E-mail: chppjc@bath.ac.uk

 The ORCID identification number(s) for the author(s) of this article can be found under <https://doi.org/10.1002/adma.202302146>

© 2023 The Authors. Advanced Materials published by Wiley-VCH GmbH. This is an open access article under the terms of the Creative Commons Attribution License, which permits use, distribution and reproduction in any medium, provided the original work is properly cited.

DOI: 10.1002/adma.202302146

M. V. Cowley, P. J. Cameron
Department of Chemistry
University of Bath
Claverton Down, Bath BA2 7AY, UK

N. Gluck
Department of Chemical Engineering
20 Research Way (Building 82)
Monash University Clayton Campus
Monash, VIC 3800, Australia

M. H. Fsadni, M. Freitag, T. J. Penfold
School of Natural and Environmental Sciences
Newcastle University
Newcastle upon Tyne NE1 7RU, UK

and often not reproducible. New tools are required to accelerate development.

Existing experimental techniques to probe the energetic alignments of a device include capacitance-voltage measurements,^[5] transient photocurrent/photovoltage measurements,^[6] electroabsorption (EA) spectroscopy,^[7] kelvin probe force microscopy (KPFM),^[8] X-ray Photoelectron Spectroscopy (XPS)^[9] and Ultra-violet Photoelectron Spectroscopy (UPS).^[9] XPS and UPS detect material work functions of single isolated layers and require measurement under vacuum conditions. They are extremely surface sensitive, making it hard to translate the determined material properties to an assembled device. Furthermore, standard linear fits to the density of states (DOS) of UPS spectra to extract the work function and band offsets often yield values that can be off by more than 0.5 eV due to the unusually low DOS at the valence band maximum (VBM) exhibited by this class of material.^[10,11] KPFM can be applied to device cross-sections but is also incredibly sensitive to surface contaminants and surface molecules which greatly lowers accuracy and reproducibility.^[8] EA assumes that the electric field within the device is uniform, which can be violated in PSCs due to vacancy distributions interacting with electric field distributions.^[12] Therefore, a new approach is required to detect changes in energetic alignments to enable fast optimization of device interfaces, with the ultimate goal of increasing power conversion efficiencies (PCEs).

A method that determines changes in band offsets, ΔE , between the perovskite and transport layers in a PSC would be one such tool. Band offsets in this context are the difference between the relevant band maximum or minimum of the transport layer and the perovskite. These quantities are important as they partially determine the efficiency of extracting photogenerated charge carriers from the device and one way of obtaining them is to characterize the electrostatic potential drop within the device. This is due to a direct dependence of the drop in electrostatic potential across the perovskite in dark and open-circuit conditions, $\Delta\phi_{psk}$, on the work functions, W of the hole and electron transport layers (HTL and ETL)

$$\Delta\phi_{psk} = W_{htl} - W_{etl} \quad (1)$$

W. Clarke, G. Richardson
Mathematical Sciences University of Southampton
Highfield, Southampton SO17 1BJ, UK

Y. Hu
Department of Chemistry and Center for NanoScience (CeNS)
LMU Munich
81377 München, Germany

M. J. Wolf
Institute of Physical Chemistry
RWTH Aachen University
52074 Aachen, Germany
E-mail: wolf@pc.rwth-aachen.de

M. J. Wolf, A. B. Walker
Department of Physics, University of Bath
Claverton Down, Bath BA2 7AY, UK
E-mail: pysabw@bath.ac.uk

P. Docampo
School of Chemistry
University of Glasgow
University P1, Glasgow G12 8QQ, UK
E-mail: pablo.docampo@glasgow.ac.uk

In the regime of Maxwell-Boltzmann validity, W for each transport layer is determined by

$$W_{htl} = E_v^{htl} - k_B T \ln \left(\frac{N_A^{htl}}{g_v^{htl}} \right) \quad (2)$$

$$W_{etl} = E_c^{etl} + k_B T \ln \left(\frac{N_D^{etl}}{g_c^{etl}} \right) \quad (3)$$

E_v^j is the valence band maximum, E_c^j the conduction band minimum, N_A^j the acceptor doping density, N_D^j the donor doping density, g_v^j the valence band effective density of states, and g_c^j the conduction band effective density of states of material j where psk is the perovskite layer. k_B is Boltzmann's constant and T is temperature. As ΔE_j for the two interfaces is given by

$$\Delta E_{htl} = E_v^{htl} - E_v^{psk} \quad (4)$$

$$\Delta E_{etl} = E_c^{psk} - E_c^{etl} \quad (5)$$

we can see that if we effectively increase or decrease E_v^j or E_c^j by, for instance by modifying the interface with a dipole layer,^[13] we will induce an equal change in both ΔE and $\Delta\phi_{psk}$. This allows us to detect changes in ΔE if we can measure $\Delta\phi_{psk}$.

$\Delta\phi_{psk}$ can be considered analogous to the built-in voltage (V_{bi}) of a device if the transport layers have a sufficient doping density to allow ohmic contact with the device contacts and there is no change in electrostatic potential within these layers away from the perovskite interface as shown in **Figure 1**. As this would be a specific instance of a PSC, we will consider the more general case where some electrostatic potential may be lost within the transport layers and discuss $\Delta\phi_{psk}$ instead of V_{bi} .

The challenge with probing PSC device energetics is mainly due to the need to decouple ionic and electronic effects. The relatively low activation energy of iodide vacancies means that during measurements at room temperature, vacancies migrate under the applied fields and modify the electric field distribution in the device,^[15] as shown by the flat electric potential profile in the perovskite bulk in **Figure 1**. This alters the electrochemical response of the device. To address this, we have used pulsed voltage protocols to separate the electronic and ionic timescales.^[16] These measurements can overcome problems associated with other methods that decouple mixed conduction; as achieving scan rates greater than 50 V s^{-1} and sourcing small currents (20 pA)^[17] can prove difficult depending on equipment; and cryogenic cooling affects both the electronic and ionic response.^[18] In pulsed voltage measurements, a preconditioning static bias voltage is applied, and the ionic defects are allowed to come to a steady-state distribution. The device is then subjected to a fast voltage pulse and the current is measured. It is assumed that the vacancies cannot redistribute on the timescale of the pulse and so are effectively "frozen" into position. If repeated for a range of voltage pulses this measurement allows the reconstruction of a current-voltage (I - V) curve for a given ion distribution.

In this work, we report a combined theoretical and experimental study on large-crystal, perfectly oriented (001) methylammonium lead iodide (MAPbI_3) based devices. We use a pulsed volt-

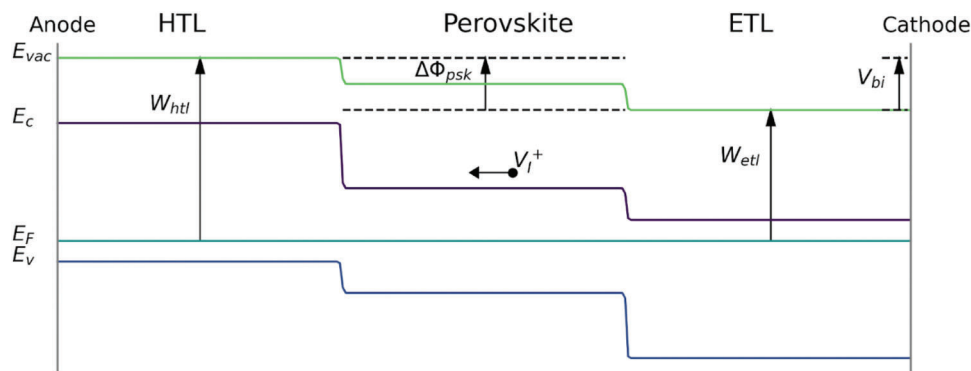


Figure 1. Schematic band diagram showing the variation in the vacuum band E_{vac} , conduction band E_c , Fermi level E_F , and valence band E_v energies across a PSC. $\Delta\phi_{psk}$ is the drop in electrostatic potential energy across the perovskite and is defined by the difference in transport layer work functions W . As there is no change in electrostatics in the transport layers, $\Delta\phi_{psk}$ is equal to the built-in voltage V_{bi} for this device. The electrostatic potential in the bulk of the perovskite is flat due to the migration of iodide vacancies V_I^+ localising charge accumulation to the interfaces.^[14]

age protocol and observe two characteristic shapes of JV curves depending on the stabilizing voltage—a preconditioning voltage that is returned to between each pulse. The drop in electrostatic potential across the perovskite is shown through drift-diffusion modeling to be measurable by quantifying the change in JV shape with stabilization voltage. This is achieved by an empirical data analysis method, where we estimate the point of change between the two characteristic JV shapes by quantifying the gradient in the JV curve around V_{oc} . This method is then shown to find values close to the theoretical drop in electrostatic potential across the perovskite and is applied to the systematic study of interfacial modifications to charge transport materials. We study the modification of band offsets using interfacial dipolar molecules and find that several proposed offset-altering molecules are unlikely to have a significant effect on the interface energetics, despite density functional theory (DFT) calculations suggesting otherwise. Our findings have important repercussions for the design of studies that aim to alter perovskite device interfaces, as well as providing a new tool that utilizes the intrinsic properties of perovskite solar cells as a diagnostic for device physics.

2. Methodology

Current-voltage scans were carried out on perovskite solar cells with the layered structure FTO/TiO₂/MAPbI₃/spiro-OMeTAD/Au. By controlling the solvent ratio of dimethyl sulfoxide (DMSO) and dimethylformamide (DMF) during the MAPbI₃ synthesis, and by adding tetrahydrothiophene-1-oxide both the grain size and crystal orientation in our perovskite films were controlled.^[19] Devices had perovskite crystal facets oriented in the (001) direction parallel to the substrate. This allows a less disordered interface, appropriate when investigating surface energetics. Previous studies have indicated different orientations of perovskite crystals can alter stability and performance as shown by Xi et al. and Figure S1 (Supporting Information).^[20] We selected the (001) orientation due to it providing the best-performing device with a uniform plane orientation. In all cases, the orientation of the perovskite crystals was verified using grazing-incidence wide-angle x-ray scattering measurements as shown in our previous works.^[21,19]

The devices show high power conversion efficiencies under standard 1 Sun illumination (AM1.5) with some hysteresis (Figure S2, Supporting Information) and high EQE spectra (Figure S3, Supporting Information). After the long-term light exposure received during measurements, the Maximum-Power-Point (MPP) was shown to be stable for more than 5 minutes (Figure S4, Supporting Information). All JV scans and pulse measurements in the rest of this work were performed using a white LED at low light intensity (approximately 20 mW cm⁻²) to minimize degradation effects caused by long measurement times.

In JV scans measured at slow and intermediate scan rates (generally below 500 mVs⁻¹), vacancies in the perovskite have time to move in response to the applied voltage during the experiment which leads to JV hysteresis. The scan rate at which maximum hysteresis is seen is related to the activation energy for the mobile ions.^[14] Material engineering that alters the activation energy for ion motion may lead to “hysteresis free” cells when they are measured at 10–200 mVs⁻¹; but unless there are minimal mobile vacancies or recombination centers in the perovskite, hysteresis will still be visible if the cells are measured over a large enough range of scan rates.^[22,23] Figure S5 (Supporting Information) shows the JV scans for a representative device performed at various scan rates under a white LED at approximately 20 mW cm⁻² which demonstrates hysteresis at several scan rates. This effect is attributed to the choice of materials (MAPbI₃ on compact TiO₂) and device architecture (non-inverted) which even for the highest-performing devices of this class, result in some degree of hysteresis.^[24]

Additionally, it is important to emphasize that, simply because a device exhibits low or no hysteresis in a particular JV curve measurement, it does not mean that there are no moving ions; rather, on the timescale of the measurement, (which depends on the scan rate used) the ionic distribution was not altered significantly or interfacial energy offsets introduced by the choice of extraction layer were able to compensate the detrimental effects of the ionic re-distribution in that timeframe.^[14] This point is also demonstrated by Cave et al.,^[25] where only the timescale at which the ionic effects are present is altered by a change in ionic migration activation energy or by Calado et al.^[26] who find evidence

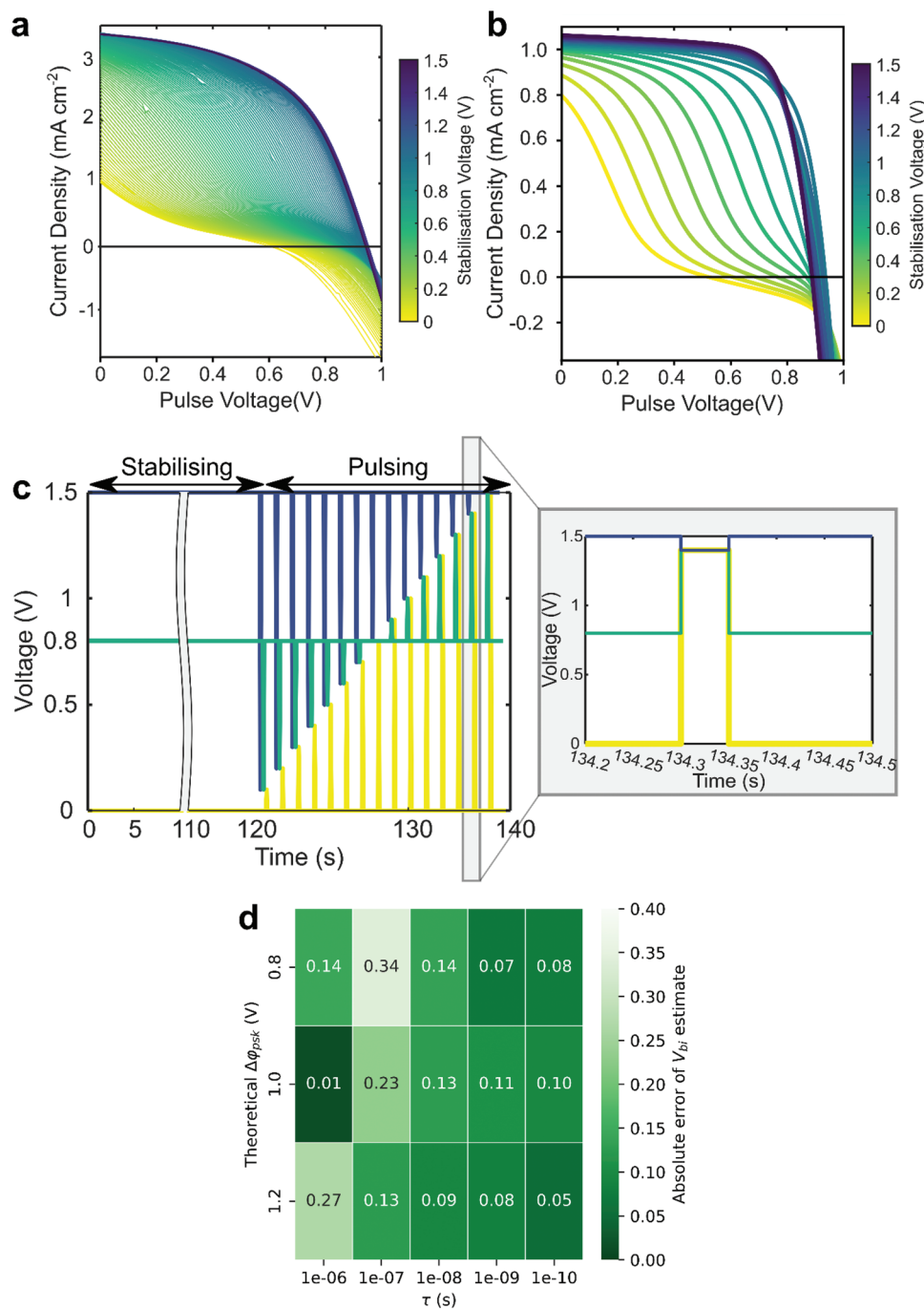


Figure 2. a) Reconstructed JV curves from the stabilize-and-pulse (SaP) measurement with changing stabilization voltage measured under $\sim 20 \text{ mW cm}^{-2}$. b) Reconstructed JV curves from SaP simulations. c) Schematic of the SaP measurement. Arrows at the top indicate the different regions of the SaP measurement. An area of the pulsing section is highlighted and zoomed in on the graph on the right. d) Quantification of SaP dJ/dV fit for a range of electron-hole Shockley-Read-Hall lifetimes (τ). Figure of merit is the absolute error in volts between extracted $\Delta\phi_{psk}$ from the simulated SaP-JV curve and the theoretical input in the model $\Delta\phi_{psk}$ across the perovskite layer. A dark shade corresponds to a better fit.

for ion migration in hybrid perovskite solar cells with minimal hysteresis.

To decouple ionic effects from electronic effects, a stabilize-and-pulse (SaP) measurement was implemented as outlined in **Figure 2a**. Similar protocols have been described previously in the literature.^[18,22,27] The device is first held at a pre-stabilization

voltage for 120 seconds, seen in **Figure 2c** as the flat continuous voltage within the stabilizing section. This is long enough for the devices fabricated in this study to reach a stable current output, indicating that ionic vacancies in the perovskite are at a steady-state distribution (**Figure S6**, Supporting Information). We used the shortest pulse width compatible with our source

meter (Keithley 2401) which is approximately 37 ms (Figure S7, Supporting Information) set by the USB connection limit, but set a measurement delay to the shortest possible value of 1 ms, therefore acquiring the current value approximately 1 ms after setting the pulse voltage. This is slow enough that geometric capacitance responses are avoided (typically present on the microsecond timescale),^[28] but fast enough that ions do not have enough time to re-distribute, i.e., Domanski et al.^[29] and Pockett et al.^[30] suggest that ions can move on timescales above >100 ms. Stabilizing the cell after each pulse for 1 s before taking the following measurement, i.e., a duty cycle of around 5%, ensures a steady-state ion configuration and a reproducible stabilized J-V curve can then be extracted. Finally, the 120 s preconditioning step (recommended by NREL^[31]) required to stabilize the current in Figure S6 (Supporting Information) suggests that the ions in our experiments will not be redistributed significantly in the timescale of $\cong 1$ ms, ensuring the validity of the measurement for our samples. The pulsing section can be seen on the right of Figure 2c, with a zoomed-in section in the inset. In principle, the short timescales over which these pulses are applied do not allow the ions to migrate significantly from their initial position, but give charge carriers enough time to be extracted from the device.^[29] At the top of each square-wave voltage pulse, the current is measured to reconstruct a JV curve at a given ionic distribution. By repeating the measurement for different stabilizing voltages, the fixed ionic distributions that affect the current response from the device can be investigated.

Figure 2a shows the reconstructed JV curves from the SaP measurement. The JV curves at different ionic distributions reveal a series of pronounced s-shaped curves with the V_{oc} changing as a function of stabilization voltage (Figure S8, Supporting Information). At small stabilization voltages (<0.3 V), the V_{oc} increases linearly with stabilization voltage and the s-shapes are extremely prominent. At stabilization voltages from 0.3 V to 0.9 V, the V_{oc} increases more slowly, and the s-shape becomes less pronounced. Eventually, at large stabilization voltages (>0.9 V), the JV curve shape looks like the ideal reverse scans shown in Figure S2 (Supporting Information) with high fill factors. The V_{oc} at these large stabilization voltages changes more slowly and decreases as the stabilization voltage approaches 1.5 V. The origin of s-shaped JV curves has been explored in perovskite-based devices both experimentally^[27,32,33] and theoretically.^[34–42] However, the exact mechanistic origins of this behavior are still under debate. The s-shaped curves measured here using the SaP routine are investigated using a drift-diffusion model.

Using the open-source drift-diffusion code IonMonger^[43,44] a $\text{TiO}_2/\text{MAPbI}_3/\text{spiro-OMeTAD}$ device was simulated with the parameter set in Supplementary Table S1. An analogous voltage protocol for the experiment was used and is presented in Figure 2b showing a good qualitative fit. The device was preconditioned at the stabilization voltage until steady state was reached before rapidly sweeping in 1 ms to the pulse voltage. During the fast voltage pulse, the ion distribution was immobilized to represent vacancies that were unable to respond to the change in applied voltage. At low stabilization voltages, the s-shape is present and at around 0.6 V the behavior changes to an ideal JV curve. Additional effects from other ionic species such as MA^+ or Li^+ are not included due to having either timescales orders of magnitude slower than the experiment^[29,45] or negligible influence

on the electrostatics due to low concentrations relative to the iodide vacancies and electronic charge carriers.^[46] no special treatment was applied to the model to account for the experimental MAPbI_3 layer being crystalline and perfectly oriented to the (001) plane, suggesting that the conclusions drawn from these measurements are not limited to the MAPbI_3 layer studied in this work, but are relevant to perovskite layers generally.

Figure S9b,c (Supporting Information) shows the iodide vacancy distribution near the ETL and the HTL, respectively, for a representative perovskite solar cell with a theoretical electric potential drop across the perovskite layer, $\Delta\phi$ of 0.6 V. As the ion distribution is made static after preconditioning, these are the ion positions for the duration of the pulse. The vacancies have adjusted their position to screen the electric field across the device. The size of the vacancy accumulation at the HTL gets smaller as the applied voltage is increased until 0.6 V, where the distribution is now almost uniform across the device. After this point, as the applied voltage is further increased, the ionic vacancies begin to accumulate at the ETL and deplete at the HTL interface instead. The difference in the shape of the accumulation and depletion regions is due to the depletion region having a lower bound of 0 m^{-3} vacancy density, representing the perfect lattice.

The physical influence the different vacancy distributions have on the device can be seen in Figure S9d (Supporting Information). This figure shows the electric potential distribution across the device at the peak of the 0.6 V pulse for each stabilization voltage. This allows us to understand the size and influence of the electric field. In this diagram, electrons are driven to more positive values of electric potential, and so a negative electric field will negatively affect carrier transport to the TiO_2 and Spiro. At low stabilization voltages, there is a large negative electric field across the perovskite layer, driving charge carriers to recombine, as shown in Figure S9e (Supporting Information). The negative bulk electric field forms to compensate for the positive interface electric fields and reduce the current density extracted from the cell. The interface fields are generated by the charge accumulation at the transport layer interfaces. Conversely, at high stabilization voltages, the vacancy distribution now results in negative electric fields at the interfaces and a large positive electric field across the perovskite layer. This manifests as a reduced recombination rate, particularly near the ETL, due to improved charge carrier separation and extraction (Figure S9e, Supporting Information).

To investigate the band alignment of the device from the SaP measurement, an empirical data analysis method for quantifying the shape of the JV curve at different stabilization voltages is required. From our simulations, we know that the change from an s-shaped JV curve to a non-s-shaped JV curve signifies the change in the sign of the electric field across the perovskite layer. Using this knowledge, we look at the gradient around the V_{oc} for each stabilization voltage. The utility of the gradient is that the degree of the s-shape can now be quantified; small gradients around V_{oc} indicate there is a large s-shaped JV curve and large gradients indicate little to no s-shape in the JV curve. Alternatively, this can be quantified by finding the preconditioning voltage at which the maximum d^2J/dV^2 for $J > 0$, $V > 0$, and $dJ/dV < 0$ changes from positive to negative, indicating there is no longer an inflection point or s-shape in the curve. The dJ/dV at V_{oc} was selected as our methodology since it performs similarly (Figure S10, Supporting

Information) and is more forgiving to noisy experimental data than the d^2J/dV^2 method (Figure S11, Supporting Information).

A trend seen throughout the energy level modifications is that dJ/dV at V_{oc} starts close to zero at small stabilization voltages, but rises rapidly at a given stabilization before reaching another plateau. Therefore, dJ/dV quantifies the change between two regimes of device behavior and the relationship of dJ/dV to the stabilization voltage can be characterized by determining the point of the change between these states. This is done by first calculating the mean dJ/dV of the flat regions and performing linear regression on the steepest section of the plot. The mean of the two intersections of this line, together with the mean steady-state values of dJ/dV before and after the regime change are used to estimate the drop in electrostatic potential across the perovskite $\Delta\phi_{psk}$.

Figure 2d shows how simulations, using the quantity extracted from this method as an estimate of $\Delta\phi_{psk}$, compare with the theoretical potential drop across the perovskite from the model inputs of the work function of the ETL and HTL. As the heatmap shows, the dJ/dV method is very effective at higher values of bulk recombination; an observation explained by the fact that sufficient recombination is required for the smaller or more negative electric fields to have an impact on the current output. A bulk pseudo lifetime of 10^{-8} s is a reasonable estimate^[11,47] and at this recombination rate the predicted $\Delta\phi_{psk}$ is underestimated by a maximum of 0.14 V. This compares favorably to the instrumental error attainable using combinations of UPS and UV-visible techniques for calculating $\Delta\phi_{psk}$ (± 0.1 eV),^[10] with the added benefit of not using surface measurements of isolated thin films that do not characterize a device. Vacuum-level discontinuities can result in $\Delta\phi_{psk}$ not being simply the difference between the transport layer work functions, highlighting the importance of being able to determine $\Delta\phi_{psk}$ from the device itself.^[12] Additionally, the density of states at a given band edge may be too low to accurately determine the energy.^[10] Inter-sample consistency of the estimated $\Delta\phi_{psk}$ is a strength of our pulse-JV methodology, allowing the detection of the impact of surface modifications on band positions within a given set of devices.

Due to the relationship between the theoretical $\Delta\phi_{psk}$, the ionic vacancy distribution, and the shape of the JV curve, the SaP measurement can be used to estimate the potential drop across the perovskite layer in devices by finding the point where the JV characteristic changes from s-shape to ideal. This method of investigating energy alignment is now utilized to examine interface modifications targeted at altering energy band offsets.

3. Results

The size of $\Delta\phi_{psk}$ can be modified by changes to the transport layer material properties, or by the addition of inter-layers that contain dipoles. In PSCs, much work has been done on adding interlayers between the ETL and the perovskite to tune charge injection and extraction.^[48] In this work, we fabricated and analyzed devices where the interface between the ETL and the perovskite layer was modified by the addition of benzoic acid (BA) derivatives. These BA molecules are expected to alter the band offsets by forming molecular dipoles at the interfaces.^[13] Upon applying the SaP measurement and the dJ/dV at V_{oc} analysis described in the methodology, we can show the degree of modification of $\Delta\phi_{psk}$

compared to the untreated TiO_2 in Figure 3a. All the interfacial modifications had little effect on $\Delta\phi_{psk}$, except for the treatment with 4-amino-BA (Figure S13, Supporting Information), despite demonstrating differences in the JV curves measured as shown by Figure S12 (Supporting Information).

These values agree with estimates of $\Delta\phi_{psk}$ or V_{bi} in the literature that range between 0.74 V and 1.25 V that are obtained from Mott-Schottky analysis,^[49–51] a technique with questionable application to perovskite devices with mobile ions.^[52] We note that a value of 1.2 V has also been supported by Kelvin probe force microscopy.^[53]

To investigate how the device would be expected to change upon altering the band offset with a dipole interlayer, Figure 3b shows a band diagram of a simulated solar cell where the ETL is modified by raising the ETL band structure in 0.05 eV increments. Like an inter-layer dipole, this creates a change in the electrochemical potential drop at the ETL/perovskite interface. The dJ/dV at V_{oc} is plotted against the stabilization voltage for this series of devices in Figure 3c. Here the color of the lines corresponds to the energy level offset, ranging between 0.3 eV (yellow) and 0.1 eV (purple). The legend shows the calculated value of $\Delta\phi_{psk}$ for the cell. We can see that the increase in $\Delta\phi_{psk}$ shown by the 4-amino-BA is well reproduced by reducing the band offset at the ETL, suggesting that this molecule does indeed form an interface-modifying dipole.

We would like to note here that the addition of molecules at a surface has effects beyond introducing an interface dipole. Charge carrier transport could be impeded, or new trap sites introduced. However, as the simple change of moving the model band structure of the ETL effectively reproduces the phenomenon seen in the 4-amino-BA device we consider it unnecessary to include these additional mechanisms.

Standard JV measurements were performed on all the devices (Figure S12, Supporting Information) with a statistical analysis of PCE shown in Figure S14a (Supporting Information). Low-performing devices were left in the sample for each modification to gain an unbiased representative distribution of performance for comparison. We observed a statistically significant improvement in PCE for the C_{60} -BA treated device due to a large improvement in the V_{oc} shown in Figure S14b (Supporting Information). C_{60} is a popular organic electron transport material, with derivatives that are strong electron acceptors which allow efficient extraction of electrons from the perovskite.^[54] The other benzoic acid molecules in this study use the same anchoring group (-COOH) as the C_{60} , however, they generally do not improve device performance in the same manner.^[55] For these small molecules, the device performance was generally worse after addition compared to the reference device, though not in a statistically significant manner.

As no change in $\Delta\phi_{psk}$ was detected in the majority of surface modifications, we modelled the benzoic acid-based molecules in dichloromethane (DCM) using PBE0/def2-sv(p) density functional theory (DFT) calculations to investigate the effect of the dipole moment on the $\Delta\phi_{psk}$ of the device. DCM was chosen as it has a similar dielectric constant as benzoic acid – providing an environment more representative of the experimental system than vacuum.^[56] The magnitudes of the dipole moments are collected in Table S2 (Supporting Information), and the direction for each molecule can be seen in Figure S15

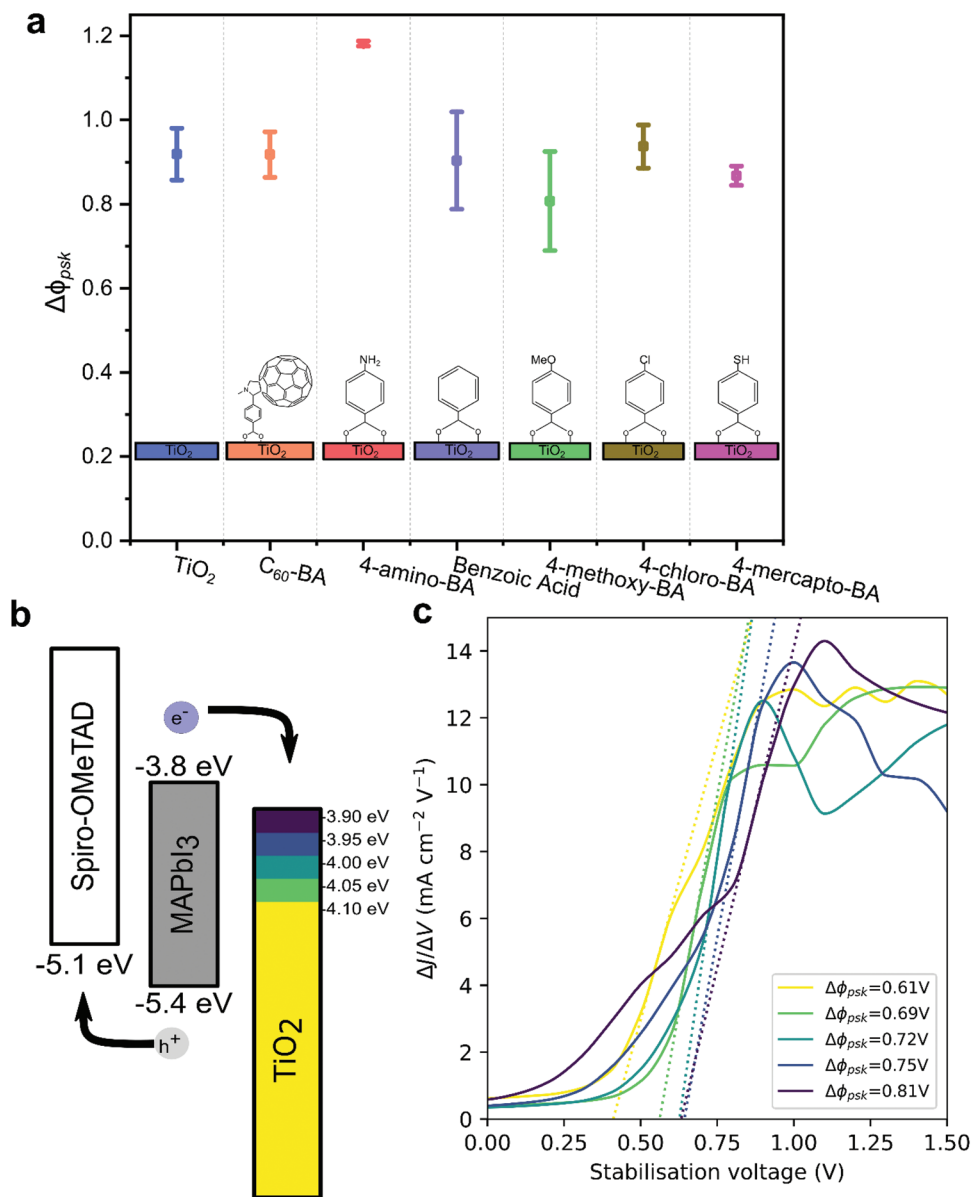


Figure 3. a) Calculated values of $\Delta\phi_{psk}$ for various benzoic acid derivative surface modifications from stabilize-and-pulse (SaP) experimental measurements. b) Schematic showing the interface band offset modifications simulated in Figure 3c. c) Effect of changing band offset on SaP simulations, where the band offset is modified from yellow (0.3 eV) to purple (0.1 eV) in 0.05 eV increments as illustrated by Figure 3b. The legend shows the calculated value of $\Delta\phi_{psk}$. The solid line corresponds to the dJ/dV quantity, and the dotted line shows the linear fit used in the calculation of $\Delta\phi_{psk}$.

(Supporting Information) indicated by the arrow. Having a dipole at the interface of the TiO_2 should act to change the energetics at the interface and hence cause the device to behave similarly to the predicted behavior shown in Figure 3b,c.

To verify this, we plotted the measured $\Delta\phi_{psk}$ against the magnitude of the dipole moment calculated from DFT [PBE0/def2-sv(p)] in Figure 4a. Here, we see no clear trend between the dipole moment and the drop in electrostatic potential across the perovskite. We propose that knowledge about the direction and magnitude of the dipole moment alone is not sufficient to explain the changes in measured $\Delta\phi_{psk}$. Although it is assumed that the benzoic acid groups anchor to the TiO_2 by the carboxylic acid group,

the exact orientation and packing are unknown.^[57,58] This supports our claims that techniques which only consider isolated interfaces and materials are not sufficient to fully explain complete device behavior.

4. Discussion

The interlayers discussed in this paper are all based on carboxylic acid anchoring groups which are well-documented to favorably bind to TiO_2 .^[57–61] Schematic diagrams of the proposed alignment of the 4-amino-BA and C_{60} -BA are shown in Figure 4b,c, respectively. Here the carboxylic acid anchoring group is bound

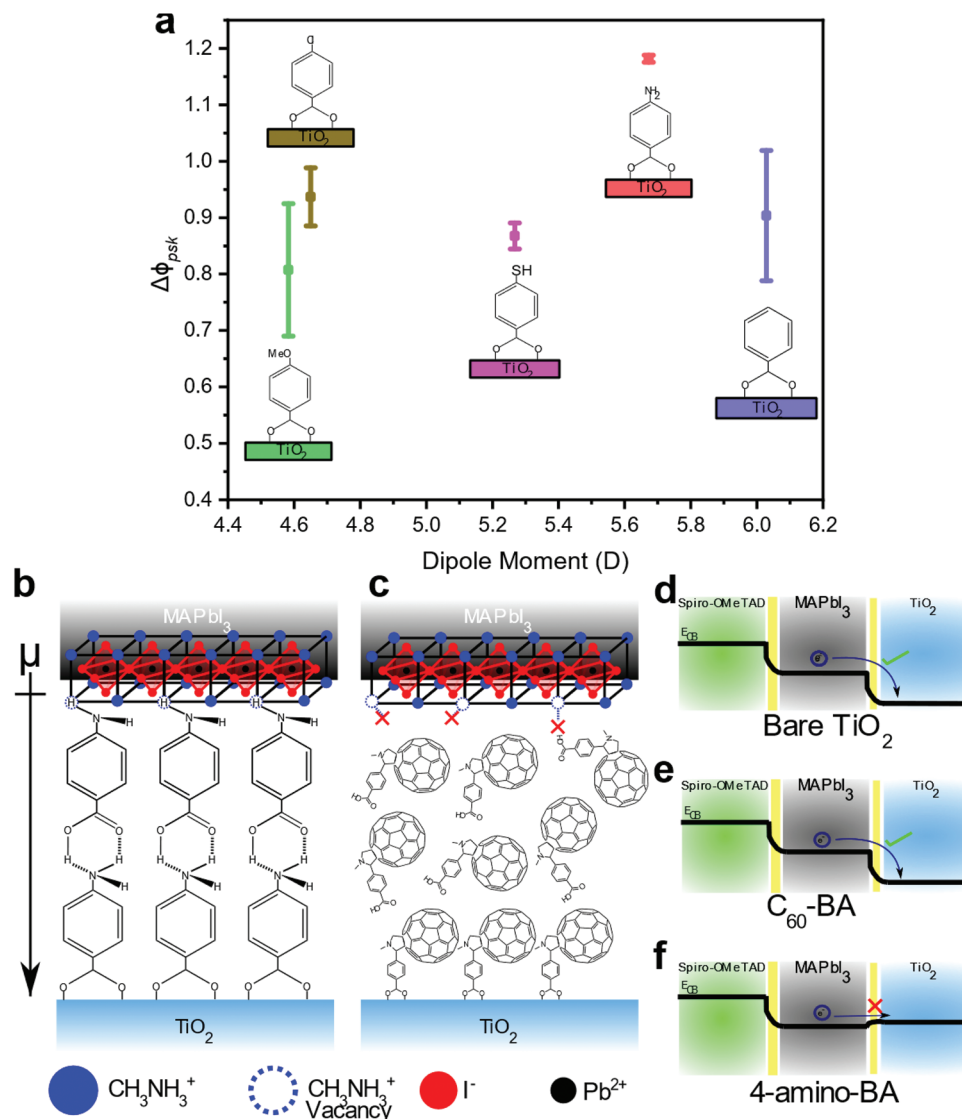


Figure 4. a) Scatterplot showing the relationship between $\Delta\phi_{psk}$ and PBE0/def2-sv(p) density functional theory computed dipole moment in dichloromethane for benzoic acid derivatives. b) Schematic diagram showing the dipole-inducing alignment of 4-amino-BA surface modification. The arrow shows the dipole orientation and interactions between the perovskite structure and other 4-amino-BA molecules are illustrated. c) Schematic diagram showing the disorder of C_{60} -BA surface modification. Dotted lines and crosses indicate non-coordination with the perovskite structure. d–f) Schematic band diagrams showing the band bending at the interface and the influence of surface modifications on device offsets for bare-TiO₂, C_{60} -BA, and 4-amino-BA, respectively.

to the TiO₂ and hence forms a uniform alignment of the surface interlayers with the TiO₂. As Noel et al. discuss, upon the annealing of CH_3NH_3 -based perovskite films, MA ions can leave the perovskite film which in turn leaves behind corresponding MA vacancies. This also leaves uncoordinated B-site and X-site atoms which results in positively charged atoms and hence favourable coordinating sites for electron-rich substituents.^[62] We hypothesize that the partially positive H atoms of the NH_2 group in 4-amino-BA will coordinate with the Pb-I lattice and hence align preferentially in the same orientation as one another. This illustrates the idea that for contact engineering to have an impact on device energetics, double-side passivation is required.^[63]

Such coordination of NH_2 groups has been experimentally verified through XPS by Liu et al. on a different amino-based interlayer.^[64] Since the method of deposition of our interlayers was through spin coating, the formation of a pristine monolayer is unlikely, and a more disordered interlayer of 4-amino-BA may exist between the bonded carboxylic acid on the TiO₂ and the coordinated NH_2 – Pb-I sites. There is likely additional hydrogen bonding between the amino group and the carboxylic acids (Figure 4b). Compared to the addition of C_{60} -BA (and the other mentioned surface modifications), where no coordination to the perovskite interface occurs (Figure 4c), the overall disorder between the TiO₂ and MAPbI₃ will be lower with 4-amino-BA. The incorporation of 4-amino-BA at this interface has been shown

to improve the morphology of the perovskite film by promoting large grain formation.^[65,66] Due to these mechanisms of interlayer ordering through surface binding of the 4-amino-BA, we propose that the overall dipole alignment is greater with this benzoic acid derivative, resulting in the observed dramatic increase in $\Delta\phi_{\text{psk}}$ when compared to the other surface interlayers.

Interestingly, molecules with the same functional groups ($-\text{NH}_2$, $-\text{COOH}$) have been shown to behave in a similar way to the 4-amino-BA. For example, 3-aminopropanoic acid bound to ZnO was confirmed by UPS to significantly modify the work function of the ZnO which allowed for a more compatible energy alignment with the perovskite.^[67] Furthermore, DFT performed by Zuo et al. on the 3-aminopropanoic acid bound to the ZnO shows a dipole moment that is oriented in the opposite direction to that shown by our DFT simulation.^[67] With this in mind, we suggest that the 4-amino-BA acts to alter the offset in our devices to an unfavorable energy alignment with the perovskite.

Figure 4d-f shows a schematic energy level diagram for the conduction band minimum (E_{CB}) through the device in three different interlayers beneath the perovskite: bare TiO_2 , C_{60} -BA and 4-amino-BA, respectively. Since there is no dipole alignment in the C_{60} -BA, no change is observed in the $\Delta\phi_{\text{psk}}$ and hence the offset between the bare TiO_2 and C_{60} -BA should remain similar. In the case of the 4-aminobenzoic acid, since the $\Delta\phi_{\text{psk}}$ measured through experimental SaP measurements (Figure 3a) is around 1.2 V, the conduction band energy of TiO_2 must increase significantly to be close to the E_{CB} of the perovskite. This offset could induce an interfacial barrier for electron extraction to the TiO_2 from the perovskite and hence cause the drop in overall device performance (Figure S12a, Supporting Information).

While the $\Delta\phi_{\text{psk}}$ in the case of the addition of C_{60} -BA does not change, a noticeable improvement in device performance is observed with a statistically significant increase in PCE and V_{oc} . This is likely due to improved charge carrier extraction from the perovskite into the TiO_2 and a reduction in surface recombination. Gao et al. suggest that the C_{60} -BA carboxylic acid group can passivate and stop the formation of trap states at the TiO_2 surface whilst C_{60} passivates surface recombination on the perovskite interface.^[68] Wojciechowski et al. show through spectroscopy measurements that there is a significant electron extraction rate increase with the addition of C_{60} -BA as compared to a bare TiO_2 interface.^[55] Similar studies in the literature all point to the improved charge collection at the TiO_2 interface, the reduction of recombination through passivation, and prolonged charge carrier lifetimes all being the reason for the systematic improvement in device performance upon the inclusion of C_{60} -BA in perovskite devices.^[67,69,70]

Similar device modifications have been investigated to find suitable interfacial materials for wide-bandgap perovskites. These provide examples of studies where a technique such as the rapid voltage pulses used in this work would have provided a systematic method to detect the proposed induced offset changes.^[71]

While this work investigates the specific case of dipole modification of the interface, the SaP methodology would be capable of detecting changes in the work function W due to doping modifications of the transport layer as shown by Equations 1–3. For example, Ding et al. attribute a change from an s-shape to an ideal diode JV curve to an increase in doping density post-oxidation of their spiro-OMeTAD layer.^[46] They simulate the result as a

change in built-in voltage. The SaP technique would allow them to experimentally test this hypothesis. We can also consider the scenario where the bulk crystal structure of the transport layer is modified to change E_{C} or E_{V} , such as in the work by Wang et al. on modified SnO_2 .^[72] In this instance, the E_{C} and W of the SnO_2 will change in tandem due to Equations 2 and 3, establishing the link between Equations 1 and 4, and making the band offset change detectable.

As a closing remark, we wish to confirm the applicability of the SaP technique to perovskite layers other than MAPbI_3 , and have performed the method on a high efficiency (>19% prior to encapsulation and ageing^[73]) triple cation solar cell and show the results in Figure S16 (Supporting Information). Here, although far less pronounced than in MAPbI_3 -based devices, there is a clear effect on the slope around V_{oc} that depends on the stabilized applied bias, as should be expected. The $\Delta\phi_{\text{psk}}$ for this device is found to be 0.91 V, which is consistent with typical $\Delta\phi_{\text{psk}}$ values in these systems.^[74] This shows that the technique is applicable even in films with reduced mobility of ionic vacancies.

Furthermore, it has been shown that devices have a measurable ionic response even after a significant reduction in mobile ion density from 10^{19} to 10^{16} cm^{-3} ,^[25] and as the highest quality perovskite thin films do not show densities below 7×10^{16} cm^{-3} , the SaP technique will still be applicable.^[75] Hence, we argue that for the majority of perovskite materials, this methodology will be readily applicable for the characterization of transport layer modifications. Additionally, the uncertainty of the extracted values (quantified by Figure 2d to be a mean absolute error of 0.09 V in $\Delta\phi_{\text{psk}}$ at $\tau = 10^{-8}$ s and below), is much preferable to the typical 0.5–1 eV error introduced by performing linear fits to the top of the VBM DOS of UPS spectra, commonly employed in the literature.^[11] While a combination of DFT to help define the VBM threshold and fits to the data employing a semilog plot can reduce this error to ± 0.1 eV, this is still comparable to the uncertainty in our developed SaP method.

5. Conclusion

Here, we have presented a novel method for determining the drop in electrostatic potential across the absorber layer in a perovskite solar cell that harnesses the presence of mobile ions and recombination sites. The stabilize-and-pulse protocol developed in this work was successful at decoupling ionic and electronic behavior. This is demonstrated by the observed change in the “s-shape” and V_{oc} of the reconstructed JV curves at different stabilization voltages, indicating that the ionic distribution can be controlled with a stabilization bias. Drift-diffusion simulations verify our findings, providing a good qualitative reproduction of the experimental data. Furthermore, the s-shape is shown to be mechanistically related to an increased recombination rate near the ETL due to a negative electric field, which drives the recombination of charge carriers.

By quantifying the change in gradient of the JV curve at V_{oc} with stabilization voltage, we can characterize the change between s-shape and diode regimes to estimate $\Delta\phi_{\text{psk}}$. For the standard architecture devices, we experimentally determined the $\Delta\phi_{\text{psk}}$ to be $0.92 \text{ V} \pm 0.06 \text{ V}$, though simulations suggest this is likely an underestimate of up to 0.2 V. Importantly, 4-amino-BA added to the surface of the TiO_2 showed that the SaP method can

measure how modifications affect the band position of the transport layers, which changes the $\Delta\phi_{psk}$ of the device, validating this approach to interfacial characterisation. No clear relationship existed between $\Delta\phi_{psk}$ and the dipole moment, indicating that conformational coverage and interactions of the dipolar molecule with the underlying TiO_2 and the perovskite are key to engineering alignment modifications. The large C_{60} -BA improves the quality and consistency of the interface, whereas the small benzoic acid derivatives do not provide the same benefit. This suggests that TiO_2 compact layers are heterogeneous and benefit from interlayers that provide a homogeneous interface, improving charge extraction.

For the first time, the mobile ion distribution in perovskite solar cells has been exploited to determine in-device energetic alignments. This opens the way to quantify the effect of novel interface engineering methods and allows systematic progress, rather than the extensive “trial-and-error” approach currently employed.

6. Experimental Section

Materials: All materials used in the experiments were purchased from Sigma-Aldrich and used as received, if not stated otherwise. Methylammonium iodide (MAI) was purchased from Greatcell Solar Ltd. 2,2',7,7'-Tetrakis [N,N-di(4-methoxyphenyl)amino]-9,9'-spirobifluorene (spiro-OMeTAD) was purchased from Luminescence Technology Corp. Glass substrates with a conducting layer of fluorine-doped tin oxide (FTO) of $8 \Omega \text{ sq}^{-1}$ sheet resistance were purchased from Yingkou Shangneng Photoelectric Material Co., Ltd.

Substrate Preparation: The FTO glass substrates were pre-patterned by laser and then cleaned with a commercial soap and water, dried with nitrogen, rinsed with ethanol, and dried again with nitrogen. The compact TiO_2 layer was prepared by a sol-gel approach with a solution containing 0.23 M titanium isopropoxide and 0.013 M hydrochloric acid in isopropanol (IPA). The mixture was spin-coated dynamically on top of the substrate at 2000 rpm for 45 s, dried at 150 °C for 10 min and annealed at 500 °C for 45 min. Afterward, the substrate surfaces were treated with the benzoic acid (BA) derivatives.

Besides one, all BA derivatives were dissolved in a 2 mg mL⁻¹ concentration in ethanol, dynamically spin-coated at 2000 rpm for 20 s and annealed at 120 °C for 5 min. After the substrates cooled down, the excess BA derivatives were washed from the substrates with ethanol four times while spin-coating the substrate at 2000 rpm for 40 s.

Only the BA derivative with a C_{60} interface (4-(1',5'-dihydro-1'methyl-2'H-[5,6]fullereno-C₆₀-1h-[1,9-c]pyrrol-2'-yl)benzoic acid (C_{60} -BA)) was deposited differently, with a 0.5 mg mL⁻¹ solution in chlorobenzene (CB) and an annealing step at 100 °C for 5 min. Additionally, to achieve better wetting and nucleation of the perovskite solution, a 0.2 wt.% IPA solution of Al_2O_3 nanoparticles (Sigma-Aldrich, < 50 nm particle size, 20 wt.% in IPA) was deposited on top of the C_{60} -BA at 2000 rpm for 30 s and dried at 120 °C for 5 min.

After the surface treatment, all substrates were immediately transferred to a glovebox (GB).

Perovskite Layer Deposition: A 57 wt.% perovskite precursor solution with lead acetate (PbAc_2) and MAI in a 1:3 ratio was prepared in a DMF/DMSO (85:15) solvent mixture and dynamically spin-coated for 2 min at 5000 rpm. After spin coating, the film appears yellow/brown and transparent. The substrate was transferred right after spin-coating to the hotplate and annealed at 130 °C for 3 min.

Solar Cell Finalization: On top of the perovskite layer, a spiro-OMeTAD layer was deposited. A 72.5 mg mL⁻¹ spiro-OMeTAD solution was used in CB with 1.75 vol% of 170 mg mL⁻¹ bis(trifluoromethane)sulfonamide lithium (Li-TFSI) salt in acetonitrile and 2.88 vol% 4-tert-butyl pyridine. The solution was spin-coated (static) at 3000 rpm for 45 s. The devices were stored overnight in a desiccator to oxidize the Li-TFSI additive in spiro-

OMeTAD. After overnight storage, the electrode areas on the devices were cleaned with gamma-butyrolactone first and ethanol (EtOH) second before transfer to a glove box (GB). An 80 nm thick Au counter electrode was thermally evaporated using a shadow mask to finalize the devices under high vacuum conditions. Before removing the devices from the GB, they were sealed with a UV adhesive (Luminescence Technology Corp.) and glass slides, with a drying time of 12 min under UV light.

Characterization: For solar cell characterization, a BioLogic potentiostat and an Abet Technologies Sun 3000 class AAA were used with an AM 1.5 G spectrum at 100 mW cm⁻² to determine the photovoltaic performance of each solar cell. Non-reflective metal masks with an aperture area of 0.16 cm² were used to define the illumination area of the devices. The devices were pre-biased for 10 s at 1.2 V with 1 sun illumination and measured in 0.1 V s⁻¹ steps.

Stabilize-and-Pulse measurements were performed on a Keithley 2401 Source meter. The source delay was set to 1 ms. A Cree High Power white LED CMT194 was used as the light source, calibrated to approximately 20 mW cm⁻² using a reference diode under an AM1.5 calibrated Heliosim CL60 solar simulator.

Maximum power point tracking was performed using a Keithley 2401 Source meter under an AM1.5 Heliosim CL60 solar simulator.

EQE measurements were taken using a Bentham PVE300 Photovoltaic EQE (IPCE) and IQE solution system.

Drift-Diffusion Simulations: An open-source drift-diffusion code, Ion-Monger (V2) was used to perform the simulations in this work, the details of which can be seen in the code release paper.^[44] The parameter set is outlined in Table S1 (Supporting Information).

Density Functional Theory: Dipole moments were obtained from DFT calculations performed using the PBE and PBE0 exchange and correlation functionals, as implemented within the ORCA quantum chemistry package (Version 5.0.2).^[76,77] Throughout, a def2-sv(p) basis set was used. Calculations were performed in vacuum and DCM, the latter achieved using a conductor-like polarizable continuum model (C-PCM).

Supporting Information

Supporting Information is available from the Wiley Online Library or from the author.

Acknowledgements

N.H. and M.V.C. contributed equally to this work. N.H. was supported by the EPSRC-UKRI DTP and would like to thank Abigail Seddon for help with the interpretation of the dipole moments of benzoic acid groups. M.V.C. was supported by the EPSRC Centre for Doctoral Training in Sustainable Chemical Technologies EP/L016354/1. M.H.F. was supported by the EPSRC Centre for Doctoral Training in Renewable Energy Northeast Universities (ReNU) EP/SO23836/1. M.H.F. thanks Julien Eng for help with visualizing the dipole moments. This research made use of the Rocket High-Performance Computing service at Newcastle University. P.D. acknowledges funding from the EPSRC under grant agreement EP/T010568/1. N.G. acknowledges funding from the Australian Government through the Australian Centre for Advanced Photovoltaics (ACAP) and the Australian Research Council through the Centre of Excellence in Exciton Science (CE170100026). Y.H. acknowledges funding from the Federal Ministry of Education and Research (BMBF) under project ID 03SF0514A/B. A.B.W. would like to thank the EPSRC for funding from grant EP/SO00763/1 (Supergen Supersolar+ Network+)

Conflict of Interest

The authors declare no conflict of interest.

Data Availability Statement

The data that support the findings of this study are available from the corresponding author upon reasonable request.

Keywords

built-in potential, interfaces, modeling, perovskite, pulsed measurements

Received: March 7, 2023

Revised: April 26, 2023

Published online: June 29, 2023

- [1] J. J. Yoo, G. Seo, M. R. Chua, T. G. Park, Y. Lu, F. Rotermund, Y. K. Kim, C. S. Moon, N. J. Jeon, J. P. Correa-Baena, V. Bulović, S. S. Shin, M. G. Bawendi, J. Seo, *Nature* **2021**, 590, 587.
- [2] K. Choi, H. Choi, J. Min, T. Kim, D. Kim, S. Y. Son, G. W. Kim, J. Choi, T. Park, *Sol. RRL* **2020**, 4, 1.
- [3] Z. Yang, B. H. Babu, S. Wu, T. Liu, S. Fang, Z. Xiong, L. Han, W. Chen, *Sol. RRL* **2020**, 4, 1.
- [4] H. Pan, H. Shao, X. L. Zhang, Y. Shen, M. Wang, *J. Appl. Phys.* **2021**, 129, 130904.
- [5] H. Dong, J. Xi, L. Zuo, J. Li, Y. Yang, D. Wang, Y. Yu, L. Ma, C. Ran, W. Gao, B. Jiao, J. Xu, T. Lei, F. Wei, F. Yuan, L. Zhang, Y. Shi, X. Hou, Z. Wu, *Adv. Funct. Mater.* **2019**, 29, 1.
- [6] A. A. Syed, L. Cai, F. Zhu, *Sol. RRL* **2020**, 2000393, 1.
- [7] C. Li, S. Tscheuschner, F. Paulus, P. E. Hopkinson, J. Kießling, A. Köhler, Y. Vaynzof, S. Huettner, *Adv. Mater.* **2016**, 28, 2446.
- [8] C. S. Jiang, M. Yang, Y. Zhou, B. To, S. U. Nanayakkara, J. M. Luther, W. Zhou, J. J. Berry, J. Van De Lagemaat, N. P. Padture, K. Zhu, M. M. Al-Jassim, *Nat. Commun.* **2015**, 6, 1.
- [9] Q. Ou, Y. Zhang, Z. Wang, J. A. Yuwono, R. Wang, Z. Dai, W. Li, C. Zheng, Z. Q. Xu, X. Qi, S. Duhm, N. V. Medhekar, H. Zhang, Q. Bao, *Adv. Mater.* **2018**, 30, 1705792.
- [10] J. Endres, D. A. Egger, M. Kulbak, R. A. Kerner, L. Zhao, S. H. Silver, G. Hodes, B. P. Rand, D. Cahen, L. Kronik, A. Kahn, *J. Phys. Chem. Lett.* **2016**, 7, 2722.
- [11] T. S. Sherkar, C. Mombblona, L. Gil-Escrig, J. Ávila, M. Sessolo, H. J. Bolink, L. J. A. Koster, *ACS Energy Lett.* **2017**, 2, 1214.
- [12] P. Mantri, S. M. H. Rizvi, B. Mazhari, *Org. Electron.* **2013**, 14, 2034.
- [13] Q. Wang, C. Chueh, T. Zhao, J. Cheng, M. Eslamian, W. C. H. Choy, A. K.-Y. Jen, *ChemSusChem* **2017**, 10, 3794.
- [14] N. E. Courtier, J. M. Cave, J. M. Foster, A. B. Walker, G. Richardson, *Energy Environ. Sci.* **2019**, 12, 396.
- [15] C. Eames, J. M. Frost, P. R. F. Barnes, B. C. O'Regan, A. Walsh, M. S. Islam, *Nat. Commun.* **2015**, 6, 2.
- [16] E. A. Duijnste, J. M. Ball, V. M. Le Corre, L. J. A. Koster, H. J. Snaith, J. Lim, *ACS Energy Lett.* **2020**, 5, 376.
- [17] Y. C. Zhao, W. K. Zhou, X. Zhou, K. H. Liu, D. P. Yu, Q. Zhao, *Light Sci Appl* **2017**, 6, e16243.
- [18] H. Wang, M. Zhou, H. Luo, *ACS Omega* **2018**, 3, 1445.
- [19] N. Giesbrecht, J. Schlipf, I. Grill, P. Rieder, V. Dyakonov, T. Bein, A. Hartschuh, P. Müller-Buschbaum, P. Docampo, *J Mater Chem A Mater* **2018**, 6, 4822.
- [20] J. Xi, H. Duijm, M. Pitaro, K. Gahlot, J. Dong, G. Portale, M. A. Loi, *Adv. Funct. Mater.* **2021**, 31, <https://doi.org/10.1002/adfm.202105734>.
- [21] N. Giesbrecht, J. Schlipf, L. Oesinghaus, A. Binek, T. Bein, P. Müller-Buschbaum, P. Docampo, *ACS Energy Lett.* **2016**, 1, 150.
- [22] S. Van Reenen, M. Kemerink, H. J. Snaith, *J. Phys. Chem. Lett.* **2015**, 6, 3808.
- [23] P. Calado, A. M. Telford, D. Bryant, X. Li, J. Nelson, B. C. O'Regan, P. R. F. Barnes, *Nat. Commun.* **2016**, 7, 13831.
- [24] H. S. Kim, I. H. Jang, N. Ahn, M. Choi, A. Guerrero, J. Bisquert, N. G. Park, *J. Phys. Chem. Lett.* **2015**, 6, 4633.
- [25] J. M. Cave, N. E. Courtier, I. A. Blakborn, T. W. Jones, D. Ghosh, K. F. Anderson, L. Lin, A. A. Dijkhoff, G. J. Wilson, K. Feron, M. Saiful Islam, J. M. Foster, G. Richardson, A. B. Walker, *J. Appl. Phys.* **2020**, 128, 184501.
- [26] P. Calado, A. M. Telford, D. Bryant, X. Li, J. Nelson, B. C. O'Regan, P. R. F. Barnes, *Nat. Commun.* **2016**, 7, <https://doi.org/10.1038/ncomms13831>.
- [27] D. A. Jacobs, Y. Wu, H. Shen, C. Barugkin, F. J. Beck, T. P. White, K. Weber, K. R. Catchpole, *Phys. Chem. Chem. Phys.* **2017**, 19, 3094.
- [28] E. Von Hauff, D. Klotz, *J Mater Chem C Mater* **2022**, 10, 742.
- [29] K. Domanski, B. Roose, T. Matsui, M. Saliba, S. H. Turren-Cruz, J. P. Correa-Baena, C. R. Carmona, G. Richardson, J. M. Foster, F. De Angelis, J. M. Ball, A. Petrozza, N. Mine, M. K. Nazeeruddin, W. Tress, M. Grätzel, U. Steiner, A. Hagfeldt, A. Abate, *Energy Environ. Sci.* **2017**, 10, 604.
- [30] A. Pockett, G. E. Eperon, N. Sakai, H. J. Snaith, L. M. Peter, P. J. Cameron, *Phys. Chem. Chem. Phys.* **2017**, 19, 5959.
- [31] T. Song, D. J. Friedman, N. Kopidakis, *Adv. Energy Mater.* **2021**, 11, 1.
- [32] L. X. Shi, Z. S. Wang, Z. Huang, W. E. I. Sha, H. Wang, Z. Zhou, *AIP Adv.* **2018**, 8, <https://doi.org/10.1063/1.5021293>.
- [33] N. Tessler, Y. Vaynzof, *ACS Energy Lett.* **2020**, 5, 1260.
- [34] S. E. Chiang, J. R. Wu, H. M. Cheng, C. L. Hsu, J. L. Shen, C. T. Yuan, S. H. Chang, *Nanotechnology* **2020**, 115403, <https://doi.org/10.1088/1361-6528/ab5a02>.
- [35] B. Li, Y. Rui, J. Xu, Y. Wang, J. Yang, Q. Zhang, P. Müller-Buschbaum, *J. Colloid Interface Sci.* **2020**, 573, 78.
- [36] R. Ge, F. Qin, L. Hu, S. Xiong, Y. Zhou, *Front Optoelectron* **2018**, 11, 360.
- [37] S. Asgary, H. M. Moghaddam, A. Bahari, R. Mohammadpour, *Sol. Energy* **2021**, 213, 383.
- [38] B. Tan, S. R. Raga, K. J. Rietwyk, J. Lu, S. O. Furer, J. C. Griffith, Y. B. Cheng, U. Bach, *Nano Energy* **2021**, 82, 105658.
- [39] Y. Cheng, H. W. Li, J. Qing, Q. D. Yang, Z. Guan, C. Liu, S. H. Cheung, S. K. So, C. S. Lee, S. W. Tsang, *J Mater Chem A Mater* **2016**, 4, 12748.
- [40] M. Li, Y. M. Xie, X. Xu, Y. Huo, S. W. Tsang, Q. D. Yang, Y. Cheng, *Org. Electron.* **2018**, 63, 159.
- [41] R. A. Z. Razera, D. A. Jacobs, F. Fu, P. Fiala, M. Dussouillez, F. Sahli, T. C. J. Yang, L. Ding, A. Walter, A. F. Feil, H. I. Boudinov, S. Nicolay, C. Ballif, Q. Jeangros, *J Mater Chem A Mater* **2020**, 8, 242.
- [42] F. Xu, J. Zhu, R. Cao, S. Ge, W. Wang, H. Xu, R. Xu, Y. Wu, M. Gao, Z. Ma, F. Hong, Z. Jiang, *Sol. Energy Mater. Sol. Cells* **2016**, 157, 981.
- [43] N. E. Courtier, J. M. Cave, A. B. Walker, G. Richardson, J. M. Foster, *J Comput Electron* **2019**, 18, 1435.
- [44] W. Clarke, L. J. Bennett, Y. Grudeva, J. M. Foster, G. Richardson, N. E. Courtier, *J Comput Electron* **2022**, <https://doi.org/10.1007/s10825-022-01988-5>.
- [45] C. Eames, J. M. Frost, P. R. F. Barnes, B. C. O'Regan, A. Walsh, M. S. Islam, *Nat. Commun.* **2015**, 6, <https://doi.org/10.1038/ncomms8497>.
- [46] C. Ding, R. Huang, C. Ahläng, J. Lin, L. Zhang, D. Zhang, Q. Luo, F. Li, R. Österbacka, C. Q. Ma, *J Mater Chem A Mater* **2021**, 9, 7575.
- [47] Z. Ni, C. Bao, Y. Liu, Q. Jiang, W.-Q. Wu, S. Chen, X. Dai, B. Chen, B. Hartweg, Z. Yu, Z. Holman, J. Huang, *Science (1979)* **2020**, 367, 1352.
- [48] K. G. Lim, S. Ahn, T. W. Lee, *J Mater Chem C Mater* **2018**, 6, 2915.
- [49] X. Zhou, J. Qiu, J. Li, W. Qi, Y. Li, S. Jiao, H. Ling, P. Wang, F. Liu, K. Sohail, J. Li, G. Wang, X. Chen, G. Hou, J. Luo, X. Zhang, Y. Zhao, Y. Li, X. Zhang, *J. Power Sources* **2022**, 518, 230734.
- [50] A. Guerrero, E. J. Juarez-Perez, J. Bisquert, I. Mora-Sero, G. Garcia-Belmonte, *Appl. Phys. Lett.* **2014**, 105, 133902.
- [51] L. Zhang, J. Gao, Z. You, Q. Li, M. Liu, Z. Ma, Y. Liu, *J Mater Chem C Mater* **2022**, 10, 16781.
- [52] O. Almora, C. Aranda, E. Mas-Marzá, G. Garcia-Belmonte, *Appl. Phys. Lett.* **2016**, 109, 173903.
- [53] C.-S. Jiang, M. Yang, Y. Zhou, B. To, S. U. Nanayakkara, J. M. Luther, W. Zhou, J. J. Berry, J. van de Lagemaat, N. P. Padture, K. Zhu, M. M. Al-Jassim, *Nat. Commun.* **2015**, 6, 8397.

- [54] K. G. Lim, S. G. Ji, J. Y. Kim, T. W. Lee, *Small Methods* **2020**, *4*, 1.
- [55] K. Wojciechowski, S. D. Stranks, A. Abate, G. Sadoughi, A. Sadhanala, N. Kopidakis, G. Rumbles, C. Z. Li, R. H. Friend, A. K. Y. Jen, H. J. Snaith, *ACS Nano* **2014**, *8*, 12701.
- [56] A. Yurquina, M. E. Manzur, P. Brito, R. Manzo, M. A. A. Molina, *J. Mol. Liq.* **2003**, *108*, 119.
- [57] M. Gliboff, L. Sang, K. M. Knesting, M. C. Schalnau, A. Mudalige, E. L. Ratcliff, H. Li, A. K. Sigdel, A. J. Giordano, J. J. Berry, D. Nordlund, G. T. Seidler, J.-L. Brédas, S. R. Marder, J. E. Pemberton, D. S. Ginger, *Langmuir* **2013**, *29*, 4176.
- [58] R. Helmy, A. Y. Fadeev, *Langmuir* **2002**, *18*, 8924.
- [59] Y. Chen, W. Liu, C. Ye, L. Yu, S. Qi, *Mater. Res. Bull.* **2001**, *36*, 2605.
- [60] Y. Zhou, Y. Shi, F. Bin Wang, X. H. Xia, *Anal. Chem.* **2019**, *91*, 2759.
- [61] A. Connell, P. J. Holliman, M. L. Davies, C. D. Gwenin, S. Weiss, M. B. Pitak, P. N. Horton, S. J. Coles, G. Cooke, *J. Mater. Chem. A* **2014**, *2*, 4055.
- [62] N. K. Noel, A. Abate, S. D. Stranks, E. S. Parrott, V. M. Burlakov, A. Gorieli, H. J. Snaith, *ACS Nano* **2014**, *8*, 9815.
- [63] F. H. Isikgor, S. Zhumagali, L. V. T. Merino, M. De Bastiani, I. McCulloch, S. De Wolf, *Nat. Rev. Mater.* **2022**, *8*, 89.
- [64] N. Liu, Q. Du, G. Yin, P. Liu, L. Li, H. Xie, C. Zhu, Y. Li, H. Zhou, W. Bin Zhang, Q. Chen, *J Mater Chem A Mater* **2018**, *6*, 6806.
- [65] B. Li, Y. Chen, Z. Liang, D. Gao, W. Huang, *RSC Adv.* **2015**, *5*, 94290.
- [66] Y. Ogomi, A. Morita, S. Tsukamoto, T. Saitho, Q. Shen, T. Toyoda, K. Yoshino, S. S. Pandey, T. Ma, S. Hayase, *J. Phys. Chem. C* **2014**, *118*, 16651.
- [67] L. Zuo, Z. Gu, T. Ye, W. Fu, G. Wu, H. Li, H. Chen, *J. Am. Chem. Soc.* **2015**, *137*, 2674.
- [68] Z. W. Gao, Y. Wang, W. C. H. Choy, *Adv. Energy Mater.* **2022**, *12*, <https://doi.org/10.1002/aenm.202104030>.
- [69] A. A. Said, J. Xie, Q. Zhang, *Small* **2019**, *15*, <https://doi.org/10.1002/smll.201900854>.
- [70] Y. Bai, Q. Dong, Y. Shao, Y. Deng, Q. Wang, L. Shen, D. Wang, W. Wei, J. Huang, *Nat. Commun.* **2016**, *7*, 1.
- [71] P. Caprioglio, J. A. Smith, R. D. J. Oliver, A. Dasgupta, S. Choudhary, M. D. Farrar, A. J. Ramadan, Y.-H. Lin, M. G. Christoforo, J. M. Ball, J. Diekmann, J. Thiesbrummel, K.-A. Zaininger, X. Shen, M. B. Johnston, D. Neher, M. Stolterfoht, H. J. Snaith, *Nat. Commun.* **2023**, *14*, 932.
- [72] P. Wang, B. Chen, R. Li, S. Wang, N. Ren, Y. Li, S. Mazumdar, B. Shi, Y. Zhao, X. Zhang, *ACS Energy Lett.* **2021**, *6*, 2121.
- [73] Y. Hu, E. M. Hutter, P. Rieder, I. Grill, J. Hanisch, M. F. Aygüler, A. G. Hufnagel, M. Handloser, T. Bein, A. Hartschuh, K. Tvingstedt, V. Dyakonov, A. Baumann, T. J. Savenije, M. L. Petrus, P. Docampo, *Adv. Energy Mater.* **2018**, *8*, 1703057.
- [74] Y. Guo, *Front Chem* **2022**, *10*, <https://doi.org/10.3389/fchem.2022.928712>.
- [75] L. Bertoluzzi, C. C. Boyd, N. Rolston, J. Xu, R. Prasanna, B. C. O'Regan, M. D. McGehee, *Joule* **2020**, *4*, 109.
- [76] F. Neese, *Wiley Interdiscip. Rev. Comput. Mol. Sci.* **2012**, *2*, 73.
- [77] F. Weigend, R. Ahlrichs, *Phys. Chem. Chem. Phys.* **2005**, *7*, 3297.